LETTERS

Adaptive subwavelength control of nano-optical fields

Martin Aeschlimann[1], Michael Bauer[2], Daniela Bayer[1], Tobias Brixner[3], F. Javier García de Abajo[4], Walter Pfeiffer[5], Martin Rohmer[1], Christian Spindler[3] & Felix Steeb[1]

Adaptive shaping of the phase and amplitude of femtosecond laser pulses has been developed into an efficient tool for the directed manipulation of interference phenomena, thus providing coherent control over various quantum-mechanical systems[1–10]. Temporal resolution in the femtosecond or even attosecond range has been demonstrated, but spatial resolution is limited by diffraction to approximately half the wavelength of the light field (that is, several hundred nanometres). Theory has indicated[11,12] that the spatial limitation to coherent control can be overcome with the illumination of nanostructures: the spatial near-field distribution was shown to depend on the linear chirp of an irradiating laser pulse. An extension of this idea to adaptive control, combining multiparameter pulse shaping with a learning algorithm, demonstrated the generation of user-specified optical near-field distributions in an optimal and flexible fashion[13]. Shaping of the polarization of the laser pulse[14,15] provides a particularly efficient and versatile nano-optical manipulation method[16,17]. Here we demonstrate the feasibility of this concept experimentally, by tailoring the optical near field in the vicinity of silver nanostructures through adaptive polarization shaping of femtosecond laser pulses[14,15] and then probing the lateral field distribution by two-photon photoemission electron microscopy[18]. In this combination of adaptive control[1–10] and nano-optics[19], we achieve subwavelength dynamic localization of electromagnetic intensity on the nanometre scale and thus overcome the spatial restrictions of conventional optics. This experimental realization of theoretical suggestions[11–13,16,17,20] opens a number of perspectives in coherent control, nano-optics, nonlinear spectroscopy, and other research fields in which optical investigations are carried out with spatial or temporal resolution.

Figure 1 schematically illustrates our approach to subwavelength optical field control: polarization-shaped ultrashort laser pulses (Methods) illuminate a planar nanostructure, with two-photon photoemission electron microscopy (PEEM)[18] providing the feedback signal from the nanoscale field distribution that is essential for adaptive near-field control. We note that the spatial resolution of two-photon PEEM (~50 nm) is determined by the electron optics and thus independent of the electromagnetic light-field diffraction limit, and that the sensitivity of the two-photon PEEM patterns to the optical field intensities arises from the nonlinear two-photon photoemission process being proportional to the time-integrated fourth power of the local electric-field amplitude (Methods). With these elements in place, a user-specified nanoscopic optical field distribution is realized by processing recorded photoemission patterns in an evolutionary algorithm that directs the iterative optimization of the irradiating laser pulse shape. The basic idea of the experiment is that the measured PEEM pattern identifies the origin of ejected photoelectrons and hence the regions of high local field intensity; controlled variation of the PEEM pattern then proves the spatial control over the nanoscopic field distribution.

The nanostructures we use consist of circular Ag disks with 180 nm diameter and 30 nm height, fabricated by electron-beam lithography on a conductive, 40-nm-thick indium-tin oxide (ITO) film grown on a quartz substrate. The disks are arranged into three dimers that form the arms of a star-like shape (Fig. 1, lower right). The whole nanostructure is about 800 nm across, while the gap between two of the dimer disks is 10 nm wide. After inspection by scanning-electron microscopy (SEM), the sample is mounted in the ultrahigh-vacuum PEEM set-up. The deposition of a small amount of caesium (~0.1 monolayers) reduces the work function of the Ag nanostructure to about 3.1 eV, that is, just below the threshold for two-photon photoemission with 790 nm photons.

Figure 2a shows the photoemission pattern obtained under illumination of the nanostructure with p-polarized femtosecond

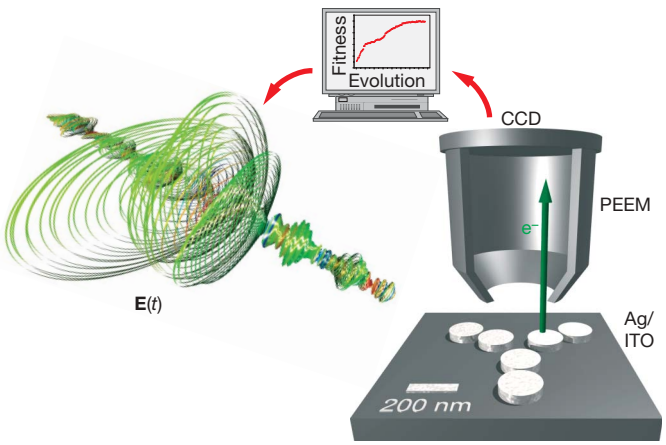

Figure 1 | Experimental scheme. A polarization shaper for ultrashort laser pulses controls the temporal evolution of the vectorial electric field **E**(*t*) on a femtosecond timescale. These pulses illuminate a planar nanostructure in an ultrahigh-vacuum chamber that is equipped with a photoemission electron microscope. The nanostructure consists of six circular Ag islands on an indium-tin oxide (ITO) film and a quartz substrate. A computer-controlled charge-coupled device (CCD) camera records the photoemission image and provides a feedback signal for an evolutionary learning algorithm. Iterative optimization of the pulse-shaper settings leads to an increase in the fitness value and correspondingly allows control over the nano-optical fields.

[1]Fachbereich Physik, Technische Universität Kaiserslautern, Erwin-Schrödinger-Str. 46, 67663 Kaiserslautern, Germany. [2]Institut für Experimentelle und Angewandte Physik, Universität Kiel, Leibnizstr. 19, 24118 Kiel, Germany. [3]Physikalisches Institut, Universität Würzburg, Am Hubland, 97074 Würzburg, Germany. [4]Instituto de Optica-CSIC, Serrano 121, 28006 Madrid, Spain. [5]Fakultät für Physik, Universität Bielefeld, Universitätsstr. 25, 33516 Bielefeld, Germany.

laser pulses (centre wavelength 790 nm, spectral full-width at half-maximum 24 nm, repetition rate 75 MHz, maximum flux 25 μJ cm^{-2}, angle of incidence 65°, projected direction of incidence **k** indicated by the white arrow). The relative geometric position of the nanostructure with respect to the two-photon PEEM image is indicated by white circles; it was established in a separate procedure by comparing the SEM image of a periodic array of nanodisk star structures with the corresponding topographic PEEM image recorded in one-photon photoemission using ultraviolet light (further information concerning this alignment, as well as SEM and ultraviolet-PEEM images, are provided in Supplementary Fig. S1). The two-photon PEEM pattern (Fig. 2a) exhibits three maxima in the photoemission yield, which are located near the inter-disk gaps in the dimers where the near-field enhancement is expected to be strongest[21]. The maximum photoelectron emission is observed from the bottom (downward-oriented) dimer, but significant contributions are seen from all three arms of the nanostructure.

We define two photoelectron emission regions as indicated in Fig. 2a by yellow squares: region A is the sum over two squares covering the upper nanostructure arms, while region B consists of one square covering the lower arm. The integral two-photon photoemission yields from these two areas reflect the local optical field intensities, which allows us to demonstrate adaptive near-field control by first maximizing, and in a second experiment minimizing, the emission ratio A/B through polarization pulse shaping directed by the evolutionary algorithm (Methods). The evolution of the photoemission contrast (A − B)/(A + B) as a function of generation number is shown in Fig. 2b for pulses shaped for maximization (red) and minimization (blue), as well as for unshaped test pulses (black) that monitor experimental fluctuations. The relatively constant level of the test signal indicates stable conditions, while optimization results in a significant increase (or decrease) of the photoemission contrast with respect to unshaped, linearly p-polarized laser pulses.

The PEEM pattern obtained after A/B maximization (Fig. 2c) shows strong emission from the two upper arms of the nanostructure and almost no emission from the bottom part, which had provided the highest count rate when using unshaped laser pulses (Fig. 2a). Analogously, the photoemission after A/B minimization (Fig. 2d) occurs mainly in the lower area while the contribution from the upper two arms is extremely weak. The adaptively determined solution to each optimization problem is robust with respect to slight imperfections in the experimental nanostructures, as discussed in Supplementary Information. These successful optimizations demonstrate that polarization pulse shaping allows adaptive control of the spatial distribution of photoelectrons on a subwavelength scale, and thus of the nanoscopic optical fields that induce photoemission.

The optimally polarization-shaped laser pulses after adaptive A/B maximization and minimization are shown in Fig. 2e and f, respectively, as determined by dual-channel spectral interferometry[14,15]. In this representation, the shape of the quasi-three-dimensional figure indicates the temporal evolution of the polarization state of the electric field, with the colour representing the momentary oscillation frequency[14] (a less intuitive but more quantitative representation is provided and discussed in Supplementary Fig. S2). Contributions from both transverse polarization components are visible in each of the two cases. Whereas the A/B maximization is achieved with a comparatively simple time evolution, the A/B minimization requires a more complex field with varying degrees of ellipticity, orientation and temporal amplitudes.

For comparison purposes, we also recorded PEEM patterns using pulses with simple polarization states characterized by only one pulse-shaping parameter. Here, a uniform spectral phase Φ_0 is assigned for one polarization component while keeping the spectral phase for the second component at zero. If no optical elements were present between the pulse-shaping liquid-crystal display (LCD) and the nanostructure, this would correspond to a simple wave plate with phase retardance Φ_0. In contrast to the adaptive optimization

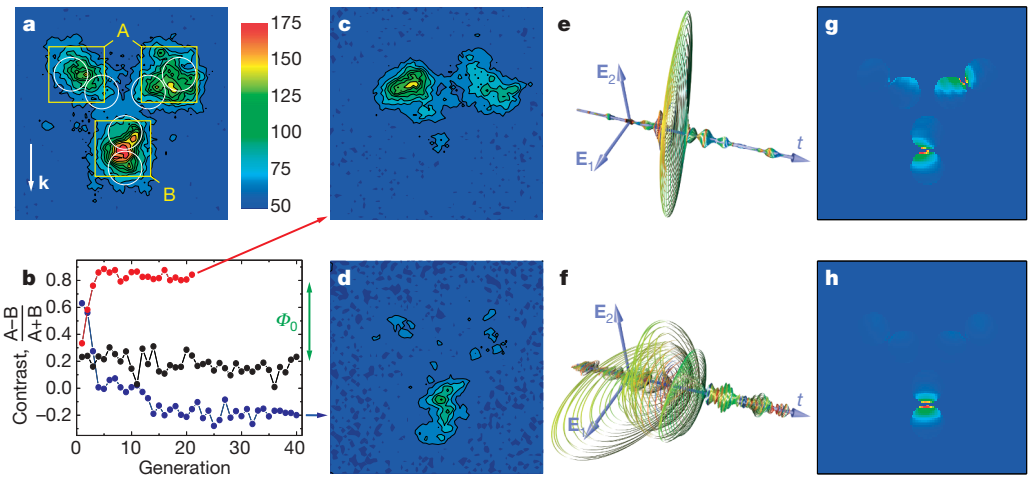

Figure 2 | Nanoscopic field control. **a**, The experimental photoelectron distribution is displayed on a 1.13 μm × 1.13 μm square for p-polarized excitation of the star-shaped nanostructure with laser pulses at 790 nm. This distribution acts as a reference for the optimization experiments with complex polarization-modulated laser pulses. The colour scale bar represents the photoemission yield in arbitrary units with negligible dark events but including the read-out noise of about 50. The white arrow indicates the projected direction of incidence **k** (incidence angle 65°). The nanostructure positions are marked by white circles, and the regions of interest A and B by yellow squares. **b**, Adaptive optimization of the A/B photoemission ratio leads to increased (red) and decreased (blue) contrast of electron yields from the upper and lower regions as compared to unshaped laser pulses recorded as a reference (black). For comparison, the range of contrast variation achieved by non-adaptive single-parameter scanning of the spectrally constant phase offset between the two pulse-shaper polarization components (green arrow) is smaller and does not provide the same degree of control. **c**, The experimental PEEM image after adaptive A/B maximization using complex polarization-shaped laser pulses (fittest individual of the final generation) shows predominant emission from the upper region. **d**, Photoemission after A/B minimization is concentrated in the lower region. **e**, **f**, The optimal laser pulses as experimentally characterized display complex temporal electric-field evolution for the maximization (**e**) and minimization (**f**) objectives. E_1 and E_2 indicate the two field components that are phase-modulated in the polarization pulse shaper in the first and second LCD layer, respectively. They are at ±45° angles with respect to p-polarization. The overall time window shown is 2 ps. **g**, **h**, The simulated two-photon photoemission pattern for the experimental pulse shapes in the cases of A/B maximization (**g**) and minimization (**h**) qualitatively confirm the experimentally demonstrated nano-optical field control.

experiment, the temporal evolution of polarization and field amplitude is now not adjustable. The contrast variation accompanying the Φ_0 scan is indicated by an arrow in Fig. 2b (see Supplementary Fig. S3 for the complete curve and Supplementary Fig. S4 for a comparison of pulse shapes in Poincaré ellipticity–orientation phase space[22]). Contrast variation is achieved, but the extreme values do not match those reached with adaptive optimization, especially in the case of contrast minimization.

To further substantiate nano-optical field control, we calculated the local electric field for the nanostructure (Fig. 1) and optimized laser pulse shapes (Figs 2e and f) used in the experiments. We solve the frequency-dependent Maxwell equations rigorously by means of the boundary-element method[23,24], taking into account the precise geometry and frequency-dependent dielectric function of the nanostructure, propagation/retardation effects, and the ultrafast time-varying vectorial nature of the incident laser pulse (Methods). This yields the vectorial electric near field as a function of frequency with nanometre spatial resolution, and Fourier transformation delivers the field in the time domain. The two-photon photoemission process is then approximately modelled by calculating the fourth power of the local temporal field one nanometre below the surface of the Ag islands (that is, close to the region from which the photoelectrons actually originate), and integrating over the time period of the laser pulse. Outside the Ag structures, the emission yield is set to zero, as the electron emissivity of the ITO substrate is strongly diminished compared to Ag.

The emission distributions calculated for the optimized laser pulses of Fig. 2e and f are shown in Fig. 2g and h, respectively. Theory predicts photoelectron emission to be concentrated near the gaps between the closely spaced Ag islands, as observed experimentally (Fig. 2a). The larger spatial extent of the experimental distributions as compared to the theoretical ones is due to the limited PEEM resolution of about 50 nm and topographic effects in the photoemission process influencing the emission pattern, whereas the calculation has a grid resolution of 9.3 nm. This is also the reason why only one peak is seen for each of the 'dimer' structures in the experimental PEEM patterns. When comparing predicted and experimentally observed emission patterns, we note that the agreement is very good in the case of A/B minimization (compare Fig. 2d and h) and moderate for the A/B maximization (compare Fig. 2c and g), where the experimentally observed emission occurs almost exclusively from the upper region of the nanostructure whereas the simulation shows a significant contribution also from the bottom part. However, we note that a comparison of the two theoretical plots clearly indicates that the switching from A/B minimization (with bottom-only photoemission, Fig. 2h) to A/B maximization is accompanied by the appearance of photoemission in upper parts of the nanostructure (Fig. 2g); that is, the calculations give the correct tendency in emission changes although the degree of control in the experiment is actually much better. We suspect that the discrepancy between theory and experiment in A/B maximization might arise from our use of a rather simple photoemission model, which uses the fourth power of the local temporal field as a rough estimate for the non-resonant two-photon excitation in an isotropic medium and neglects the influences of varying intermediate-state lifetimes, anisotropic matrix elements, inhomogeneous surface-barrier transmission over the photoelectron energy range, and in particular the role of the surface field in the final photoemission process. For example, the electric-field component normal to the material surface may play a different role from the two tangential components, whereas in the simulation we have considered the complete field. In addition, photoelectrons might also emerge from the 'side walls' of the Ag cylindrical islands, a process not considered in our calculations.

We note that control over photoemission patterns was demonstrated in a recent two-photon PEEM experiment[25] through adjustment of the temporal phase between two unshaped femtosecond excitation pulses, which corresponds to a modification of the excitation spectrum via spectral interference. In contrast, the control mechanism underlying our approach is based on adaptive modification of spectral phase and polarization direction. So far, we have controlled only the spatial degree of freedom of the optical near-field distribution because the feedback signal used for optimization is a time-integrated quantity, but the use of a time-resolved two-photon photoemission signal would readily allow the control of spatial and temporal degrees of freedom simultaneously. Adaptive near-field control is not limited to the present nanostructure. Theoretical investigations of different geometries[13,16,17,20] together with the experimental demonstration here show that this kind of control is broadly applicable.

Summarizing, we have demonstrated mapping of photoemission patterns governed by local optical near fields with nanometre resolution, and shown that optical near fields can be manipulated on a subdiffraction length scale. In effect, we have realized an ultrafast nano-optical switch or multiplexer, delivering 'packets' of electromagnetic energy at desired locations below the diffraction limit. This capability should find many applications, one example being spatial–temporal control of extended quantum systems such as coupled quantum dots or nanowires; in a quantum information processing context, such control could be used to optically and selectively address qubits that are only several nanometres apart. In plasmonic nanodevices, energy transport could be controlled on a nanometre length scale[20]. Near-field imaging techniques[26] and surface-enhanced Raman spectroscopy could also benefit from a subwavelength optimization of electromagnetic fields. The adaptive scheme also provides a femtosecond electron source with a nanoscale-controllable origin. And ultimately, spatial–temporal spectroscopy with direct nanometre and femtosecond resolution[13] might become possible, enabling the direct spatial probing of coupling and energy transfer processes on the nanoscale. Just as the introduction of adaptive femtosecond laser pulse shaping has brought significant advances to the area of coherent chemical reaction control, we expect the concept reported here to provide analogous opportunities in nanophotonics.

METHODS

Polarization pulse shaping. The femtosecond polarization pulse shaper contains a two-layer 128-pixel LCD spatial light modulator in the Fourier plane of a zero-dispersion compressor in folded 4*f* configuration[14,15]. The first and second LCD layers modulate the spectral phase of two transverse polarization components, leading to a spectral variation of polarization state and phase. Hence in the time domain, the intensity, momentary oscillation frequency, and polarization state (that is, elliptical eccentricity and orientation) can all be made to vary within a single laser pulse. In the present improved experimental set-up, we use volume-holographic gratings to achieve high diffraction efficiency for both polarization components, avoiding efficiency-compensating Brewster windows used earlier[14,15]. Experimental characterization of the polarization-shaped laser pulses proceeds directly in the beam path of the experiment via dual-channel spectral interferometry with an unshaped reference laser pulse whose spectral phase is determined separately by SPIDER[27].

Adaptive optimization. In the evolutionary algorithm[28], pulse-shape optimization occurs for both LCD layers independently. For reasons of maintaining experimental stability, the convergence rate is desired to be as high as possible, and thus the complexity of available pulse shapes was reduced by coupling together sequences of four neighbouring LCD pixels. This leads to a reduction of the overall temporal pulse-shaping window to approximately 1 ps, which is still appropriate to control two-photon photoemission without resonant (and longer-lived) intermediate levels. As we are interested in mapping photoemission with nanometre spatial resolution, the issue of long-term drifts of the sample position with respect to the PEEM detection needs to be addressed. After each generation of evolutionary optimization, a PEEM picture with an unshaped laser pulse is recorded as a reference. Performing a two-dimensional cross-correlation with the reference pattern obtained at the beginning of the experiment, the momentary drift vector is calculated automatically and extrapolated linearly to correct for the drift of each individual PEEM picture during the optimization. The good performance of this procedure is apparent from the small variations in the corrected monitoring signal (black curve in Fig. 2b).

Photoemission electron microscopy. The photoemission electron microscope uses an electrostatic lens system to map the lateral variations in the

photoemission yield from the nanostructured surface at ≤50 nm resolution[29]. After amplification using an imaging-quality micro-channel plate, the image is projected onto a screen of phosphorescent material, which is then read out by a Peltier-cooled CCD camera. This signal is used as the input for the evolutionary algorithm for pulse-shape optimization. PEEM in combination with the two-photon photoemission technique is particular sensitive to variations in the local near-field due to the fourth power dependence of the two-photon photoemission yield on the electric field amplitude[30]. The conventional contrast mechanisms of PEEM (work-function variations and topography) do not contribute to the two-photon PEEM signal from the nanostructured surface, as is evident from a direct comparison of the nanoscale structure and the two-photon photoemission yield (Fig. 2a).

Near-field calculation. In the calculations of the near-field response with the boundary-element method[23,24], retardation effects and material properties are taken into account, but the influence of the ITO layer and the quartz substrate is neglected. The vectorial near field is obtained separately for the two cases of s- and p-polarized excitation and for each frequency component of the LCD pulse-shaper pixels. Each response term is then weighted by the (complex-valued) experimentally determined polarization-shaped amplitude-and-phase factor of the incident pulse, and coherent vectorial superposition delivers the full nanoscopic field[13,16]. As only smooth focusing is employed in the experiment ($f = 33$ cm), all simulations are performed in plane-wave approximation, and tight-focusing calculations[17] are not required.

Received 12 September 2006; accepted 3 January 2007.

1. Judson, R. S. & Rabitz, H. Teaching lasers to control molecules. *Phys. Rev. Lett.* **68,** 1500–1503 (1992).
2. Assion, A. *et al.* Control of chemical reactions by feedback-optimized phase-shaped femtosecond laser pulses. *Science* **282,** 919–922 (1998).
3. Meshulach, D. & Silberberg, Y. Coherent quantum control of two-photon transitions by a femtosecond laser pulse. *Nature* **396,** 239–242 (1998).
4. Weinacht, T. C., Ahn, J. & Bucksbaum, P. H. Controlling the shape of a quantum wavefunction. *Nature* **397,** 233–235 (1999).
5. Brixner, T., Damrauer, N. H., Niklaus, P. & Gerber, G. Photoselective adaptive femtosecond quantum control in the liquid phase. *Nature* **414,** 57–60 (2001).
6. Dudovich, N., Oron, D. & Silberberg, Y. Single-pulse coherently controlled nonlinear Raman spectroscopy and microscopy. *Nature* **418,** 512–514 (2002).
7. Herek, J. L., Wohlleben, W., Cogdell, R. J., Zeidler, D. & Motzkus, M. Quantum control of energy flow in light harvesting. *Nature* **417,** 533–535 (2002).
8. Feurer, T., Vaughan, J. C. & Nelson, K. A. Spatiotemporal coherent control of lattice vibrational waves. *Science* **299,** 374–377 (2003).
9. Shapiro, M. & Brumer, P. *Principles of the Quantum Control of Molecular Processes* (Wiley-Interscience, Hoboken, NJ, 2003).
10. Brixner, T. & Gerber, G. Quantum control of gas-phase and liquid-phase femtochemistry. *ChemPhysChem* **4,** 418–438 (2003).
11. Stockman, M. I., Faleev, S. V. & Bergman, D. J. Coherent control of femtosecond energy localization in nanosystems. *Phys. Rev. Lett.* **88,** 067402 (2002).
12. Stockman, M. I., Bergman, D. J. & Kobayashi, T. Coherent control of nanoscale localization of ultrafast optical excitation in nanosystems. *Phys. Rev. B* **69,** 054202 (2004).
13. Brixner, T., García de Abajo, F. J., Schneider, J. & Pfeiffer, W. Nanoscopic ultrafast space-time-resolved spectroscopy. *Phys. Rev. Lett.* **95,** 093901 (2005).
14. Brixner, T. & Gerber, G. Femtosecond polarization pulse shaping. *Opt. Lett.* **26,** 557–559 (2001).
15. Brixner, T., Krampert, G., Niklaus, P. & Gerber, G. Generation and characterization of polarization-shaped femtosecond laser pulses. *Appl. Phys. B* **74,** S133–S144 (2002).
16. Brixner, T., García de Abajo, F. J., Schneider, J., Spindler, C. & Pfeiffer, W. Ultrafast adaptive optical near-field control. *Phys. Rev. B* **73,** 125437 (2006).
17. Brixner, T., García de Abajo, F. J., Spindler, C. & Pfeiffer, W. Adaptive ultrafast nano-optics in a tight focus. *Appl. Phys. B* **84,** 89–95 (2006).
18. Schmidt, O. *et al.* Time-resolved two photon photoemission electron microscopy. *Appl. Phys. B* **74,** 223–227 (2002).
19. Novotny, L. & Hecht, B. *Principles of Nano-Optics* (Cambridge Univ. Press, Cambridge, UK, 2006).
20. Sukharev, M. & Seideman, T. Phase and polarization control as a route to plasmonic nanodevices. *Nano Lett.* **6,** 715–719 (2006).
21. Hao, E. & Schatz, G. C. Electromagnetic fields around silver nanoparticles and dimers. *J. Chem. Phys.* **120,** 357–366 (2004).
22. Brixner, T. Poincaré representation of polarization-shaped femtosecond laser pulses. *Appl. Phys. B* **76,** 531–540 (2003).
23. García de Abajo, F. J. & Howie, A. Relativistic electron energy loss and electron-induced photon emission in inhomogeneous dielectrics. *Phys. Rev. Lett.* **80,** 5180–5183 (1998).
24. García de Abajo, F. J. & Howie, A. Retarded field calculation of electron energy loss in inhomogeneous dielectrics. *Phys. Rev. B* **65,** 115418 (2002).
25. Kubo, A. *et al.* Femtosecond imaging of surface plasmon dynamics in a nanostructured silver film. *Nano Lett.* **5,** 1123–1127 (2005).
26. Sánchez, E. J., Novotny, L. & Xie, X. S. Near-field fluorescence microscopy based on two-photon excitation with metal tips. *Phys. Rev. Lett.* **82,** 4014–4017 (1999).
27. Iaconis, C. & Walmsley, I. A. Spectral phase interferometry for direct electric-field reconstruction of ultrashort optical pulses. *Opt. Lett.* **23,** 792–794 (1998).
28. Baumert, T., Brixner, T., Seyfried, V., Strehle, M. & Gerber, G. Femtosecond pulse shaping by an evolutionary algorithm with feedback. *Appl. Phys. B* **65,** 779–782 (1997).
29. Swiech, W. *et al.* Recent progress in photoemission microscopy with emphasis on chemical and magnetic sensitivity. *J. Electron Spectrosc. Relat. Phenom.* **84,** 171–188 (1997).
30. Cinchetti, M. *et al.* Photoemission electron microscopy as a tool for the investigation of optical near fields. *Phys. Rev. Lett.* **95,** 047601 (2005).

Supplementary Information is linked to the online version of the paper at www.nature.com/nature.

Acknowledgements We thank S. Fechner and G. Krampert for constructing the improved pulse shaper, and the Nano-Bio Center at the University of Kaiserslautern for support in the preparation of the nanostructures. This work was supported by the German Science Foundation (DFG) within an Emmy Noether research group (T.B.), by the Graduiertenkolleg 792 (F.S.), and by the Spanish MEC (F.J.G.A.).

Author Contributions The principal investigators of this work are M.B., T.B., F.J.G.A. and W.P.

Author Information Reprints and permissions information is available at www.nature.com/reprints. The authors declare no competing financial interests. Correspondence and requests for materials should be addressed to T.B. (brixner@physik.uni-wuerzburg.de).